Hindawi
Structural Control and Health Monitoring
Volume 2023, Article ID 4093158, 16 pages
https://doi.org/10.1155/2023/4093158

Research Article

Measurement Accuracy Analysis of Distributed Fiber Optic Sensors for Asphalt Mixture Based on the DEM-FDM Coupled Method

Zejiao Dong[1], **Jiwen Zhang**[1], **Xianyong Ma**[1] and **Han Zhao**[2]

[1]*School of Transportation Science & Engineering, Harbin Institute of Technology, Harbin 150090, China*
[2]*Department of Road Engineering, Jilin Traffic Planning and Design Institute, Changchun 130021, China*

Correspondence should be addressed to Zejiao Dong; hitdzj@hit.edu.cn

Received 23 September 2022; Accepted 17 October 2022; Published 8 February 2023

Academic Editor: Francesc Pozo

Distributed fiber optic sensors (DFOSs) have been effectively used for pavement health monitoring. However, the inhomogeneity of the asphalt mixture and the characteristics of the sensor affect the measurement accuracy, which in turn affects the performance evaluation of asphalt pavement. In this study, the strain of nonembedded DFOS specimens was used as a reference and compared with the strain of embedded DFOS specimens to analyze the accuracy of DFOS based on the four-point bending test. To further improve accuracy, a numerical simulation model was established by coupling the discrete element method (DEM) and the finite difference method (FDM), and feasibility of the model was verified by comparing it with the load-displacement curves obtained from laboratory tests. The results of the laboratory tests and numerical simulations showed a linear relationship between the reference strain and the DFOS strain. Therefore, a strain correction method was proposed for the DFOS based on the DEM-FDM method, and the strain correction coefficient was used as the evaluation index. In addition, an orthogonal test was performed to analyze the influence of design parameters, including elastic modulus, section height, and section width, on the accuracy of the DFOS. Through variance and range analysis, it was found that elastic modulus has a significant effect on the strain measurement accuracy, followed by the section height and the section width. In summary, this study proposed an efficient strain correction method suitable for the application of DFOS in pavements considering the material characteristics of the asphalt mixture and the embedded sensor.

1. Introduction

In recent years, the health monitoring of transportation infrastructure has received increasing attention. Pavement health monitoring interprets the connection between external loads and internal response by placing sensors within the pavement structure and analyzing the monitoring data collected. It has provided many new methods for pavement mechanics verification, structural design, and maintenance decisions [1–3].

The optical fiber sensor is an important sensing element, which is used in pavement health monitoring. It has the advantages of high sensitivity, strong anti-interference ability, and corrosion resistance. The most common components include fiber Bragg grating sensors, which are known for high-precision testing, but they can only monitor small areas near the sensor. As an emerging sensing technology, DFOSs can measure physical parameters distributed along the whole length of the optic fiber axis. The distributed optical fiber sensing technique is based on three types of light scattering in optical fibers, namely, Brillouin scattering, Raman scattering, and Rayleigh scattering. Among them, the optical frequency-domain reflectometry (OFDR) technique is based on Rayleigh scattered light and has the characteristics of high spatial resolution and high strain accuracy [4, 5]. The OFDR technique has been frequently used in structural health monitoring, especially concrete durability testing [6, 7], crack development process monitoring and

quantification [8, 9], and concrete-reinforcement interaction behavior [10, 11].

Before testing the optical fiber sensors, strain calibration coefficients are usually obtained from calibration tests for subsequent correction of test results [12–14]. Some fiber optic sensors need to be embedded in the host material during testing, and the traditional calibration tests cannot accurately describe the true relationship between the sensor and the host material. On one hand, the force mode is different from the calibration test, and on the other hand, the sensor embedding method, the properties of the host material, and the encapsulation material of the sensor affect the accuracy of the embedded sensor during testing [15, 16]. Therefore, many scholars have investigated the interaction and strain transfer mechanism between fiber optic sensors and host materials, including theoretical, experimental, and simulation approaches. From the theoretical perspective of the strain transfer, various multilayer strain transfer models have been proposed based on shear hysteresis theory to provide strain transfer coefficients [17–21]. The advantage of this method is that the results are clear, but the mechanical model is simple and not accurate enough for complex loading states and structural materials. From the perspective of laboratory testing, the testing scheme has been improved to enhance the accuracy of calibration coefficients. The main change is that the test object contains the sensor and the host material, so their interaction is also considered [22]. The test results are more intuitive, but the process is slow and laborious. From the perspective of numerical simulation, the most dominant method is the finite element method, followed by the discrete element method, whose main purpose is to analyze the synergistic deformation of the sensor and the host material, to validate the proposed strain transfer model, and to achieve the optimal design of the sensor [21, 23–25]. Compared with theoretical methods, numerical simulation methods can consider more complex stress states and materials and are more convenient than laboratory test methods, which are selected as the main research tool in this paper.

For pavement health monitoring [26–30], it is necessary to embed DFOSs in asphalt mixture. However, the effect of this behavior on the surrounding physical field and the measurement accuracy of DFOSs still needs further study. Therefore, it is important to choose a suitable research method. In theoretical and finite element analyses, the host material is assumed to be continuous, whereas the asphalt mixture is usually an inhomogeneous material, and this assumption obviously affects the results. The DEM-FDM method is a numerical simulation method that combines the discrete element method with the finite difference method. Currently, this method is used to simulate track and ballast in railway engineering [31, 32]. In geotechnical engineering, it is also used to study slope supports and soils [33, 34]. In this paper, the DEM-FDM method can simultaneously consider the discrete characteristics of asphalt mixture and the continuous characteristics of DFOS, which is more conducive to the analysis of the problem.

The objective of this paper is to investigate the strain measurement accuracy of the DFOSs for pavement health monitoring. Firstly, static loading four-point bending tests were performed on nonembedded and embedded DFOSs mixtures. Secondly, a coupled DEM-FDM numerical simulation method was used for modeling based on the discrete characteristics of the asphalt mixture and the continuous characteristics of DFOS. The feasibility of this method was verified by comparing with the laboratory test results. The reference strain and the DFOS strain were compared, and their relationship was analyzed to obtain a strain correction coefficient to improve sensor accuracy. Finally, considering the diversity of DFOSs, the strain correction coefficients of DFOSs with different design parameters such as elastic modulus, section height, and section width are further investigated.

2. Description of the Laboratory Tests

2.1. Materials. AC-13 asphalt mixture was designed according to the Chinese "Technical Specification for Highway Asphalt Pavement Construction" (JTG F40-2004) [35]. The binder used was 70# base asphalt, and the characteristics of the base asphalt are provided in Table 1. The combined gradation of the aggregate is shown in Table 2, and the gradation curve is shown in Figure 1. Based on the Marshall mix design method, the optimum asphalt content, bulk density, and air voids of the AC-13 asphalt mixture were determined as shown in Table 3.

2.2. Sensors. The optical fiber Bragg grating (FBG) sensor used unencapsulated bare fiber Bragg grating with a grating length of 15 mm. The DFOS was developed by the research group, and the bare fiber with a diameter of 125 microns was packaged with a diameter of 6 mm polyurethane elastomer. The structure and size of the DFOS are shown in Figure 2. The parameters of encapsulation materials are shown in Table 4.

FBG sensor data were collected by using the fiber grating demodulator. The OFDR device of Luna Technology was used for data collection of DFOS. In this paper, the technical specifications adopted by the OFDR device are shown in Table 5.

For OFDR devices, a strain coefficient was required to convert Rayleigh's shift to strain. To obtain the strain coefficient, we conducted tensile calibration tests on the DFOS. The test process is shown in Figure 3, and the test data are shown in Table 6. The theoretical strain in Table 6 is the strain calculated according to the size and tensile deformation of DFOS. Rayleigh's shift was measured by using the OFDR device. The mean value of the results of the three tests was taken as the final strain coefficient.

2.3. Specimen Preparation. This paper used vertical vibration testing equipment (VVTE) [36, 37] to form asphalt mixture specimens (400 mm × 100 mm × 100 mm). The design of VVTE mimics the internal vibratory structure of the vibratory roller, which is sufficient to simulate the compaction effect during the construction of the real pavement structure.

Table 1: Characteristics of 70# base asphalt.

Property	Value
Penetration (25°C, 100 g, 5 s, 0.1 mm)	76.3
Softening point (°C)	43
Viscosity (180°C, Pa·s)	0.39
Density (25°C, g/cm^3)	1.03

Table 2: Aggregate gradations of AC-13.

Sieve size (mm)	16	13.2	9.5	4.75	2.36	1.18	0.6	0.3	0.15	0.075
Passing percentage (%)	100.0	96.3	76.8	51.0	37.7	27.6	19.2	13.0	8.1	5.6

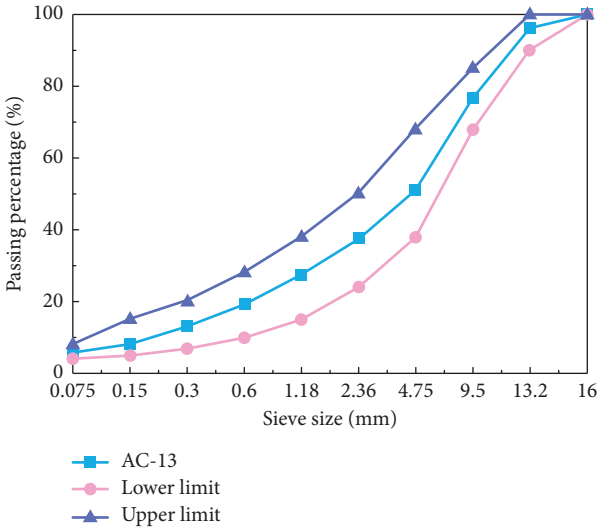

Figure 1: Mixture gradation of AC-13 employed.

Table 3: Properties of the AC-13 asphalt mixture.

Mixture	Asphalt content (%)	Bulk density (g/cm^3)	Air voids (%)
AC-13	4.8	2.452	4.2

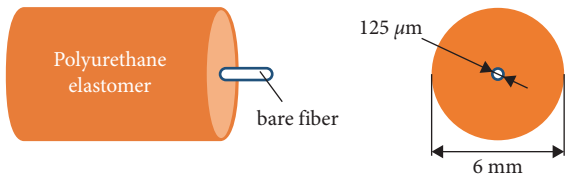

Figure 2: Structure and size of DFOS.

Table 4: The parameters and data sources of encapsulation material.

Material parameters	Value	Data sources/Reference
Elastic modulus	3000 MPa	Tensile test (GB/T 2567–2008)
Poisson ratio	0.25	Manufacturer information
Density	1080 kg/m^3	Manufacturer information

To compare the effect of the embedded DFOS on the asphalt mixture, two conditions were designed. Condition I is the control or reference asphalt mixture specimen. After

Table 5: The technical specifications of the OFDR device.

Parameter	Specification
Spatial resolution	2.6 mm
Sampling frequency	250 Hz
Strain measurement range	±12,000 $\mu\varepsilon$
Strain resolution	1 $\mu\varepsilon$
Instrument strain accuracy	±1 $\mu\varepsilon$

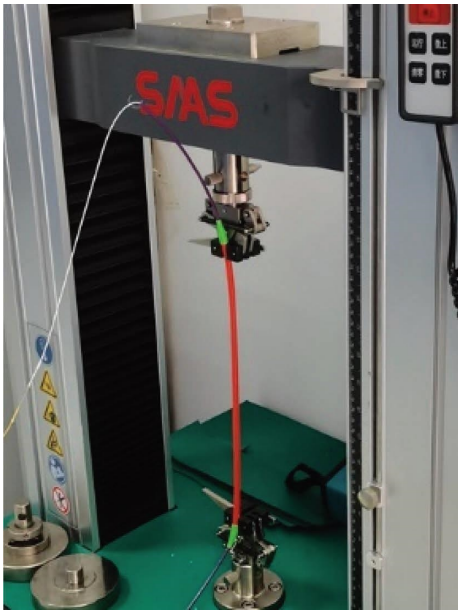

Figure 3: Tensile calibration test of DFOS.

Table 6: Calculation of the strain coefficient of DFOS.

Theoretical strain (μm/m)	Measured Rayleigh's shift of the DFOS (GHz)			
	1	2	3	Mean
338.983	−39.152	−36.594	−38.562	−38.103
677.966	−79.864	−77.523	−79.864	−79.084
1016.949	−122.659	−122.048	−124.437	−123.048
1355.932	−165.871	−170.497	−170.568	−168.978
1694.915	−216.153	−215.425	−216.915	−216.164
2033.898	−252.783	−258.972	−261.143	−257.633
2372.881	−296.444	−300.435	−305.824	−300.901
Strain coefficient (μm/m·GHz)	−8.04	−7.94	−7.86	−7.95

the specimen is demoulded, we pasted an unencapsulated FBG sensor in the midspan 20 mm from the bottom of the beam to test the strain of the reference specimen. If the adhesive material is coated on the FBG sensor, its survival rate and test accuracy are affected. Therefore, epoxy resin was applied on both sides of the Bragg grating when the FBG sensor was pasted, as shown in Figure 4(a). Because the length of FBG grating is 15 mm, we set the distance of epoxy resin paste points as 20 mm. Condition II is the asphalt mixture beam with embedded DFOS; that is, the DFOS is installed in advance during the asphalt mixture forming process. The mold used in this condition has holes in the side for penetrating the DFOS. To ensure that the DFOS sensor was located 20 mm away from the bottom of the beam, asphalt mixture was covered twice, as shown in Figure 5.

The sensors involved in the two conditions above are strain sensors, but the strains tested are different. The FBG sensors bonded to the surface of the asphalt mixture beam were designed to obtain the original strain of the host material at the same location as a reference. Therefore, for the ease of memorization, the strain of the FBG sensor was referred to as the reference strain measured in the laboratory.

2.4. Four-Point Bending Test. A four-point bending test was conducted to simulate the actual pavement internal tensile state condition. In this test, the beam specimen is subjected to a vertical load and the beam is deformed under the action of the bending moment. To study the effectiveness of the DFOSs for testing in asphalt mixtures [38], this study selected the four-point bending test as the main test method.

In the four-point bending test, the center distance of the loading roller was 100 mm, and the center distance of the supporting roller was 300 mm. To simulate the impact effect of a vehicle on an actual road structure, the instantaneous load was applied to the beam specimen by using an electronic universal testing machine. The loading process was carried out at a speed of 50 mm/min in the displacement-controlled mode. When the vertical displacement of the loading roller was 0.3 mm, the loading process was carried out ten times as one step. The load-displacement curves and sensor data under different loads were recorded. Five tests were carried out for each condition.

3. DEM-FDM Numerical Simulation

3.1. Coupled Model Modeling. Mastic theory considers the asphalt mixture as a multistage spatial mesh structure of the dispersion system [39]. It is a coarse dispersion system with a coarse aggregate as the dispersed phase and dispersed in the asphalt mortar medium. The mortar is a fine dispersion system with a fine aggregate as the dispersed phase and dispersed in the asphalt mastic medium. The mastic is a microdispersion system with fillers as the dispersed phase and dispersed in the high consistency asphalt medium.

The supporting role of the fine aggregate and mineral powder on the asphalt mixture skeleton is small. Especially when the fine aggregate and mineral powder are coated with asphalt, it is difficult to reflect their own strength. Therefore, the aggregates above 2.36 mm and 2.36 mm below were used as coarse aggregates and asphalt and mineral powder unified as asphalt mortar, respectively, and the voids were considered to model the asphalt mixture.

Condition I does not involve a DFOS, so only the discrete element method was used to build the DEM model. The modeling process is more complicated in Condition II because of the DFOS. Unlike the discrete characteristics of the asphalt mixture, the DFOS is continuous. Considering the characteristics of different materials, discrete element software Particle Flow Code (PFC) was used to describe the characteristics of asphalt mixture, and finite difference software Fast Lagrangian Analysis of Continuum (FLAC) is used to describe the DFOS to build the coupled DEM-FDM model. The modeling process of condition I and condition II is similar, and the differences in the process are shown in Figure 6.

Taking the more complex DEM-FDM coupling model as an example, the specific modeling process is introduced as follows [40]. In the modeling process, each stage of the model is described as follows and is also shown in Figure 7:

(1) Establishment of specimen space: according to the actual size of the specimen, the forming mold space with wall command was established, and space was reserved at the sensor embedding position.

(2) Generate coarse aggregate: it was assumed that the density of aggregates is equal, and we calculated the volume of the specimen occupied by a certain grade of aggregate according to the volume fraction and then divided it by the average volume of the equivalent ball rounded to obtain the number of aggregate particles in that grade. We imported multiple irregularly shaped shells as the template of clump element and generated each grade of the aggregate by the radius scaling method inside the specimen space.

(3) Generate asphalt mortar: the asphalt mortar was considered a homogeneous discrete element, which was represented by a regular homogeneous ball element of 0.5 mm radius. First, we iterated and saved the information of coarse aggregate clump elements. Then, ball elements with a radius of 0.5 mm and regular arrangement were generated within the space of the specimen. The ball elements, which were spatially located inside the clump elements, were regarded as aggregates, and the external elements were regarded as asphalt mortar. With this step, the clump elements were replaced with the ball elements; that is, the coarse aggregate was composed of a series of ball element combinations.

(4) Check the gradation: the gradation of the coarse aggregate was checked after replacing it with the ball elements. If the percentage of all the small ball particles of each grade of the aggregate to the total particles of the whole model is within a certain range of the target percentage, then the model is regenerated by adjusting the number of individual

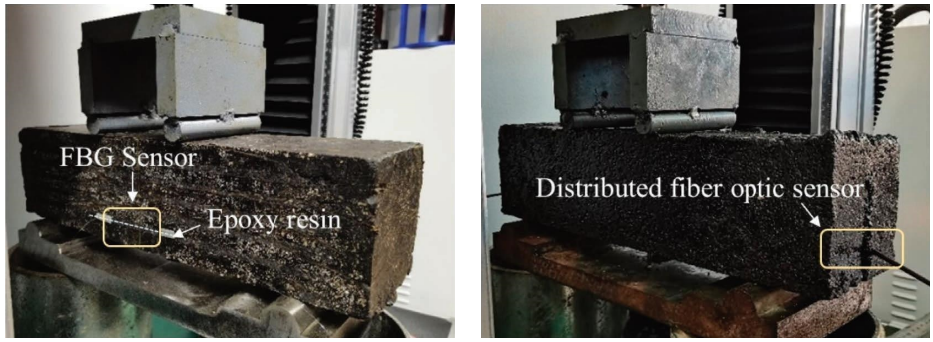

Figure 4: Diagram of laboratory test conditions. (a) Condition I: surface-bonded FBG sensor and (b) Condition II: embedded DFOS.

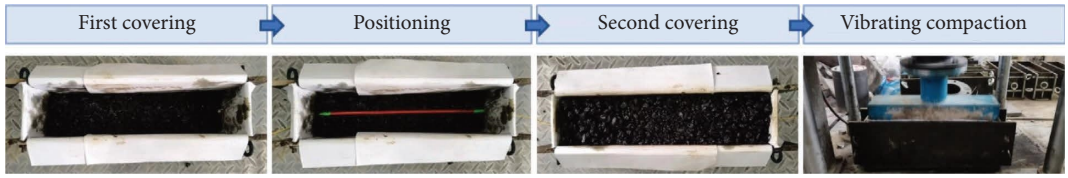

Figure 5: The molding process of the specimen with embedded DFOS.

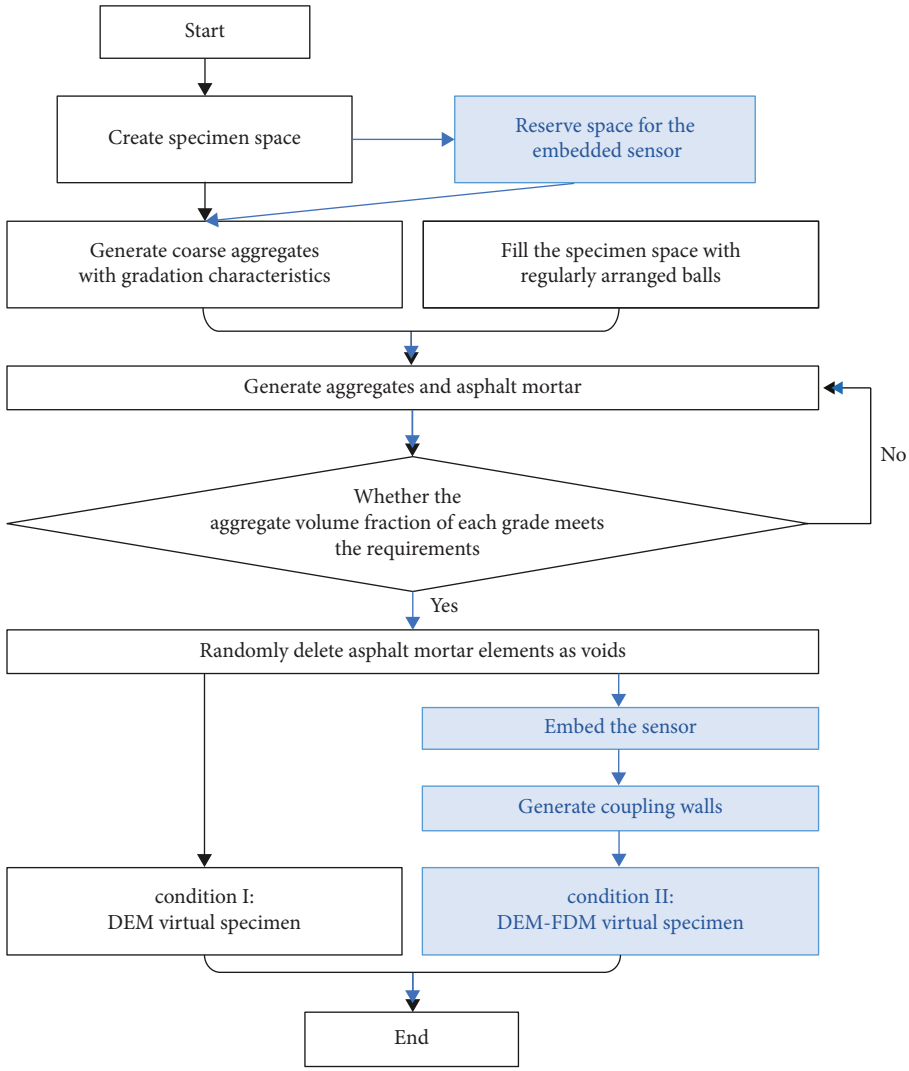

Figure 6: Modeling process of condition I and condition II using DEM-FDM numerical simulation.

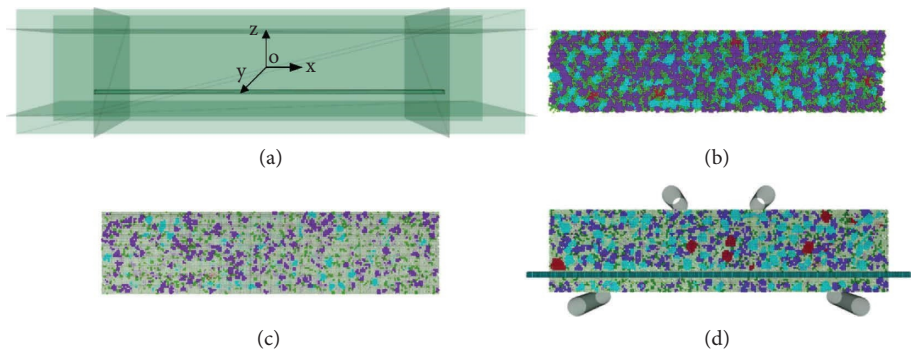

Figure 7: Specific modeling process of the DEM-FDM coupled model. (a) Specimen space. (b) Coarse aggregate. (c) Specimen. (d) DEM-FDM model (profile).

grades of the aggregate until the requirements are met.

(5) Generate the void: the number of particles of the asphalt mortar that is needed to be deleted was calculated according to the void. We randomly deleted a certain number of small balls in the asphalt mortar to create the void.

(6) Embed the sensor: we called the zone command in the FLAC module and referred to the actual size of the sensor and material properties which are shown in Table 4, and we built a DFOS virtual model with the radial-cylinder grid.

(7) Establish the coupling wall: we generated the coupling wall between the interface of the DEM model and the FDM model and cycle to a new force balance under the action of gravity to achieve sufficient interaction between discrete particles and continuum. The coupling walls were created coinciding with zone faces. Walls were composed of edge-connected triangular faces, where vertex velocities and positions were specified as a function of time. The coupling logic worked by taking the contact forces and moments with the wall facets and determining an equivalent force system at the facet vertices. These forces were transferred to the grid points along with stiffness contributions.

(8) Establish the loaded wall: according to the actual loading roller size and distance, four cylindrical walls with 20 mm diameter and 110 mm length were established at the specified position to simulate the loading roller and support roller for the subsequent loading implementation.

3.2. Contact Models. Asphalt mixture is a nonhomogeneous and anisotropic material, which mainly consists of aggregates, asphalt mortar, and voids. Therefore, the following types of contacts were considered in the discrete element model of the asphalt mixture [41, 42].

(i) The contact between asphalt mortar

(ii) The contact between the aggregate and the asphalt mortar

(iii) The internal contact of aggregates

(iv) The contact between the aggregate and other aggregates

(v) The contact between various elements and the wall

Asphalt is used as a bonding material, and the contact between asphalt mortars and between asphalt mortars and the aggregate reflects the bonding properties. In addition, in the simulation of this paper, the coarse aggregate was bonded by several spherical elements, so its internal contact also needed to be bonded. In the contact model of PFC, the Burgers model is usually used to simulate the viscoelasticity of asphalt, but the test simulated in this paper is a four-point bending test, and the Burgers model does not have tensile capacity. Thus, the linear parallel bond model was selected to describe the first three contact types. It can transfer force and moment and can describe the stress-strain characteristics of the asphalt mixture well during bending. The contact between the aggregate and the aggregate, as well as the contact between the various elements and the wall, can be regarded as linear contact considering the frictional sliding effect. Therefore, the last two contact types were chosen as the linear model. Figure 8 represents various types of contact models used.

3.3. Numerical Simulation Verification. Referring to the load-displacement curves under two working conditions obtained from the indoor tests (shown in Figure 9), the contact model parameters were adjusted repeatedly to make the simulation results close to the test results. In addition, the numerical simulation parameters of the zone elements used to simulate the DFOS are shown in Table 4. The load-displacement curve in Figure 9 shows the error bands of five tests under different working conditions.

The final contact model selection and parameter values are shown in Table 7. Five numerical simulations were carried out for each working condition, and the load-displacement curves obtained were consistent with the laboratory test results. Compared with previous studies [24, 31, 41, 43, 44], the value range of contact model parameters is similar, which verifies the rationality of numerical simulation model parameters. The slope of the curve of condition II is significantly greater than that of condition I, indicating

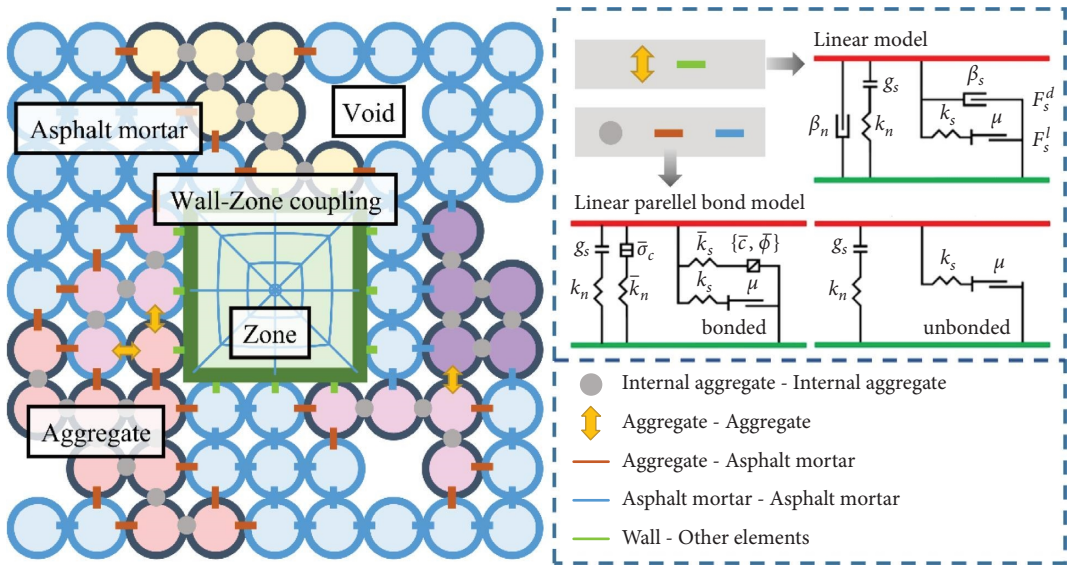

Figure 8: Schematic of the relationship between the elements of the coupled DEM-FDM model.

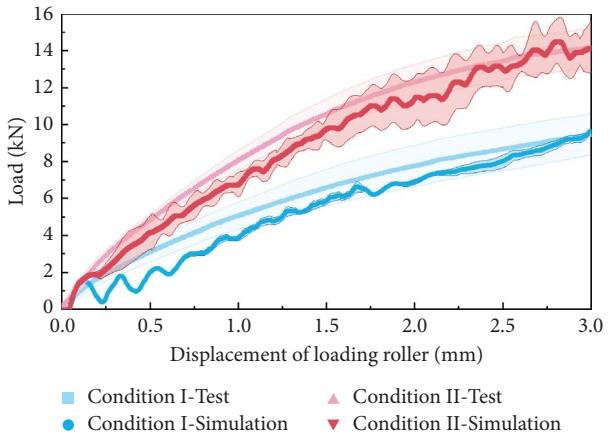

Figure 9: Load-displacement curve of the four-point bending tests.

that the bearing capacity of the asphalt mixture beam has been improved after embedding the DFOS.

4. Accuracy Evaluation Method

4.1. Reference Strain. In the numerical simulation of condition I, all the spherical elements that coincide with the core of the embedded DFOS were marked. The displacement of the spherical element under multistage loading was extracted by numerical simulation, and the axial strain was calculated as the reference strain. In laboratory test condition I, the FBG sensor test results were used as the actual field reference strain.

The reference strains obtained from numerical simulations and laboratory tests are plotted in Figure 10. The curves in Figure 10 represent the mean value of the reference strain distributed along the axial position of the specimen under step loading in the numerical simulation, and the light-colored shadows represent the error bands of the reference strain obtained by the simulation. The shape of the curve conforms to the trapezoidal distribution recognized by the four-point bending theory. The purple point represents the reference strain measured by the FBG in the middle of the beam specimen, and its error line is marked.

The mean value of the DFOS strain in the pure bending section (−50 mm~50 mm) of the specimen in the numerical simulation was extracted and compared with the FBG strain obtained in the laboratory test. The linear fitting relation is shown in Figure 11. The results show that the reference strains of the laboratory test and numerical simulation have good linear correspondence, and the numerical simulation is representative.

4.2. DFOS Strain. Condition II was further analyzed. Firstly, the measured DFOS data of the OFDR device was derived, and the laboratory test results under different load levels were extracted, as shown in Figure 12(a). In terms of DEM-FDM coupling numerical simulation, the DFOS under different load levels was characterized by the strain of the zone elements, and the strain distribution graph is drawn, as shown in Figure 12(b). Figure 12 shows that the strain distribution of the pure curved section is trapezoidal and gradually increases in laboratory tests and numerical simulations.

It can be seen that compared with the DFOS strain in the laboratory test shown in Figure 12(a), the DFOS strain curve obtained by numerical simulation in Figure 12(b) is not smooth. Since the strain information extracted in Figure 12(b) comes from the zone element, it indicates that the discrete element representing the asphalt mixture transmits its discreteness to the continuous zone element during load transfer.

The mean strain values of the pure bending section in Figure 12 were extracted and plotted in Figure 13. It can be found that the DFOS strain obtained in the laboratory test

Table 7: Contact model and values.

Contact model	Symbol	Parameter	Unit	Value
Internal aggregate (linear parallel bond model)	E^*	Effective modulus	N/m^2	$2e9$
	$\overline{E^*}$	Bond effective modulus	N/m^2	$5e8$
	$\overline{\sigma_c}$	Tensile strength	MPa	$6e8$
	$\overline{c}$	Cohesion	MPa	$3e8$
	$\overline{\kappa^*}$	Bond normal-to-shear stiffness ratio	—	2.5
	μ	Friction coefficient	—	0.5
Aggregate-aggregate (linear model)	E^*	Effective modulus	N/m^2	$2e9$
	κ^*	Normal-to-shear stiffness ratio	—	2.5
	μ	Friction coefficient	—	0.5
Asphalt mortar-asphalt mortar (linear parallel bond model)	E^*	Effective modulus	N/m^2	$4.8e8$
	$\overline{E^*}$	Bond effective modulus	N/m^2	$1.2e8$
	$\overline{\sigma_c}$	Tensile strength	MPa	$1.4e7$
	$\overline{c}$	Cohesion	MPa	$7e6$
	$\overline{\kappa^*}$	Bond normal-to-shear stiffness ratio	—	3.0
	μ	Friction coefficient	—	0.5
Aggregate-asphalt mortar (linear parallel bond model)	E^*	Effective modulus	N/m^2	$4.8e8$
	$\overline{E^*}$	Bond effective modulus	N/m^2	$1.2e8$
	$\overline{\sigma_c}$	Tensile strength	MPa	$1.26e5$
	$\overline{c}$	Cohesion	MPa	$6.3e5$
	$\overline{\kappa^*}$	Bond normal-to-shear stiffness ratio	—	3.0
	μ	Friction coefficient	—	0.5
Wall-other elements (linear model)	k_n	Normal stiffness	N/m	$1e8$
	k_s	Shear stiffness	N/m	$1e8$
	μ	Friction coefficient	—	0.5

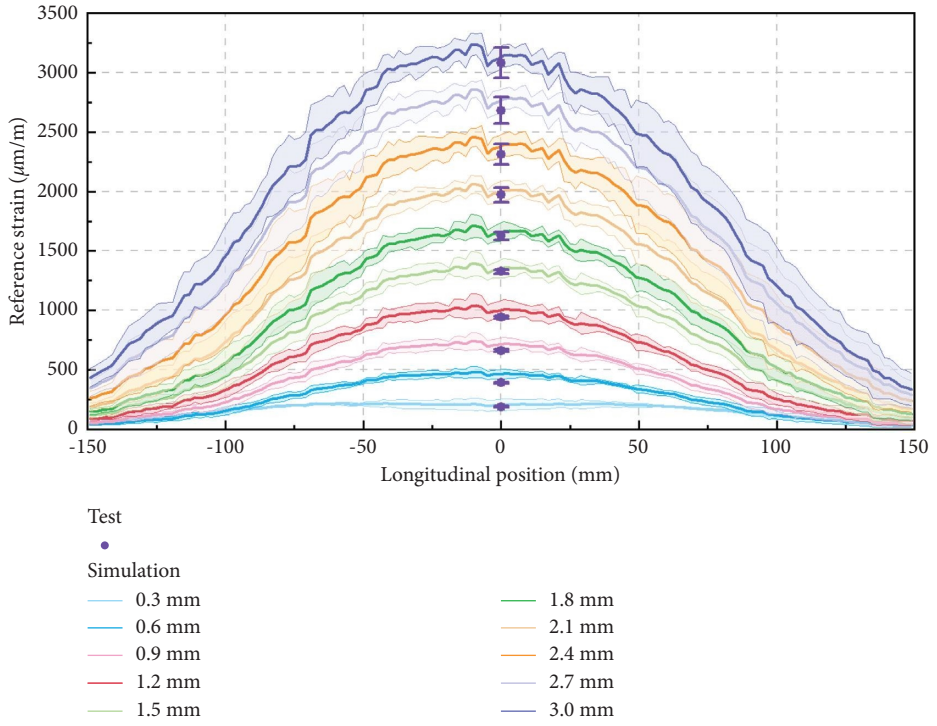

Figure 10: Reference strain in laboratory tests and numerical simulations under different vertical displacements of loading rollers.

and numerical simulation also has a good linear relationship. Therefore, the numerical simulation method can better reproduce the laboratory test process and results.

4.3. Strain Correction Method. In order to further explore the relationship between the DFOS strain and the reference strain, Figure 14 was drawn. It can be found that the

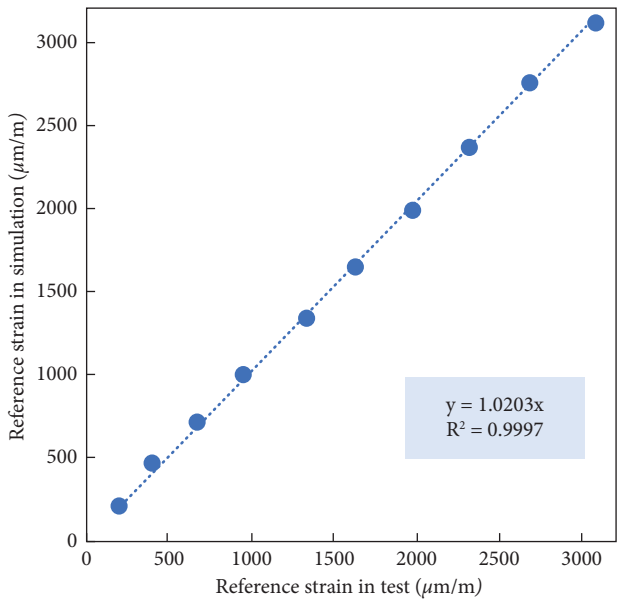

Figure 11: Linear relationship between the reference strain of the pure bending section in laboratory tests and numerical simulations.

development trends of the reference strain and DFOS strain are consistent in both numerical simulations and laboratory tests, but the strain values are different. Considering the load-displacement curve shown in Figure 9, comprehensive analysis shows that the carrying capacity of the asphalt mixture specimens increases after embedding the DFOS, indicating that the embedded DFOS will disturb the physical field of the asphalt mixture. In the use of sensors, on the one hand, we should avoid such a situation in the selection of sensors. On the other hand, in order to ensure the effectiveness of strain testing, the DFOS strain needs to be corrected.

A linear relationship between the DFOS strain and the reference strain was established in the tests and simulations, as shown in Figure 15. The linear fitting correlation between the DFOS strain and the reference strain indicates that the strain of the embedded DFOS can be corrected by a linear relationship, and the slope of the linear relationship is the strain correction coefficient.

The strain correction coefficient of the laboratory test is 1.4132, and the strain correction coefficient of the numerical simulation is 1.4086, which are relatively close. It can be concluded that the coupled DEM-FDM numerical simulation can not only restore the physical field around the DFOS but also can be used for the correction of the strain test results.

In order to ensure the reliability of the strain correction coefficient obtained by this method, the numerical simulation parameters were not changed, only the loading roller distance was changed to simulate different test conditions. The numerical simulation conditions with loading roller distances of 5 cm and 15 cm were added, and 5 groups of tests were set for each condition. It can be seen from Figure 16 that both the reference strain and DFOS strain value decrease as the loading roller distance increases. According to the linear relationship analysis in Figure 17, when the loading roller distance is 5 cm and 15 cm, the strain correction coefficients obtained by numerical simulation are 1.4317 and 1.3972, respectively. This value is similar to 1.4086 when the distance between loading rollers is 10 cm. It can be seen that under different test conditions, the reference strain and DFOS strain show the same variation trend, and the strain correction coefficient is similar, which confirms the accuracy of the strain correction coefficient. In practical applications, the mean value of the strain correction coefficient under different conditions can be used to correct the DFOS strain.

5. Factors Affecting Accuracy

5.1. Orthogonal Test Design. Previous analysis shows that the carrying capacity of the asphalt mixtures was improved after the DFOS with the elastic modulus of 3 GPa and a cross-sectional diameter of 6 mm was embedded in the asphalt mixture. The strain value measured by this DFOS was less than the reference strain, and the strain correction factor was greater than 1. Considering the diversity of DFOS, in order to improve the accuracy of DFOS, the influence of different design parameters on the accuracy of DFOS was further studied by the orthogonal experimental design method.

Orthogonal experimental design is a design method to study the multifactors and multilevels [45, 46]. It is based on the orthogonality to select some representative points from the comprehensive experiment for testing. These representative points satisfy the following two characteristics: first, in each column, different numbers appear equally; that is, for any factor, the number of experiments at different levels is the same. Second, in any two columns, two numbers in the same row form an ordered number pair, and each kind of number pair occurs the same number of times; that is, any two factors are cross-grouping comprehensive experiment. Orthogonal experimental design is an efficient, rapid, and economical experimental design method.

In this paper, elastic modulus, section height, and section width are selected to study. The elastic modulus was determined to be 300 MPa~3 GPa. The section width and height were determined from 4 mm to 10 mm according to the section size of common sensors. In this paper, each factor was set at four levels, and the factors and levels are shown in Table 8.

The strain correction coefficient was used as the index of investigation, and the L16 (43) orthogonal table was selected to conduct numerical simulation tests under different working conditions with the strain correction coefficient as the investigation index. In all working conditions, the numerical simulation parameters of the asphalt mixture remained unchanged, and only the sensor parameters were changed. The orthogonal test scheme and results are shown in Table 9.

5.2. Variance Analysis. The goal of variance analysis was to analyze whether there is a correlation between the independent variables and the result variables or whether

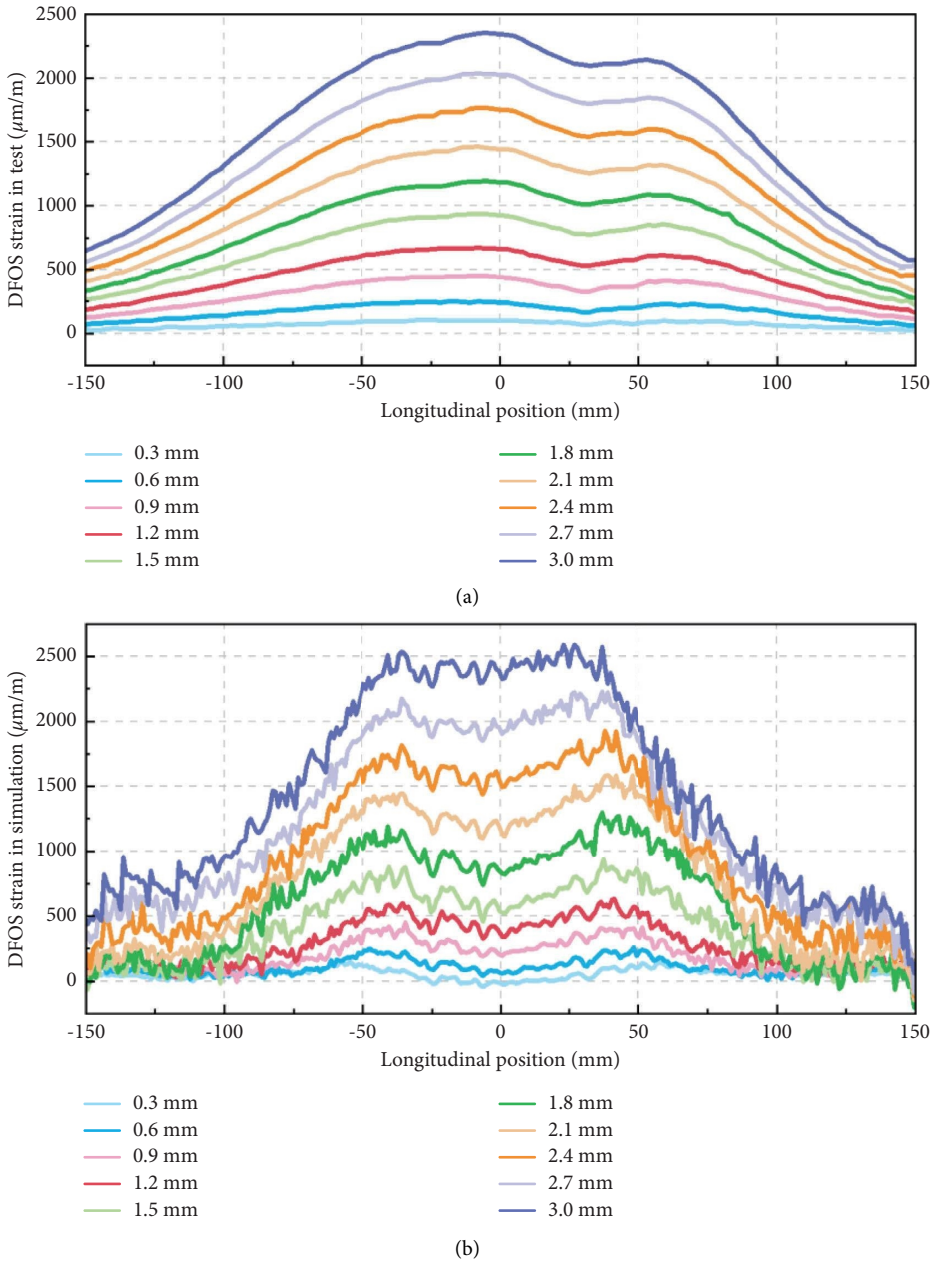

Figure 12: DFOS strain in the laboratory test and numerical simulation under condition II for example. (a) Laboratory test and (b) numerical simulation.

different levels of independent variables will lead to significant differences in the value of result variables.

According to the result of the orthogonal test, the sum of squares (SS), degrees of freedom (df), mean square (MS), and F value of each factor were calculated. The specific calculation method is shown in Table 10.

Here, to facilitate expressions, factors A, B, and C correspond to elastic modulus, section width, and section height, respectively. A total of n tests were conducted in the orthogonal experimental design, and y was the result of each test. There were a levels of factor A, and n_{Ai} tests were conducted for each level. SSA, df$A$, and MSA, respectively, represent the sum of squares, degrees of freedom, and mean square of factor A. The notation of factors B and C is similar to that of factor A.

The distribution of the F value follows the F distribution, so the F value has the corresponding significant probability p value on the F distribution. When the p value is greater than the significance level of the hypothesis test, it indicates that there is no significant difference between the intergroup variance and intragroup variance, and that is to say, different levels of factors do not influence the data as a whole. On the contrary, when the p value is less than the significance level of the hypothesis test, it indicates that different levels of factors have an overall impact on the data. The significance level can be represented by "$*$," as shown

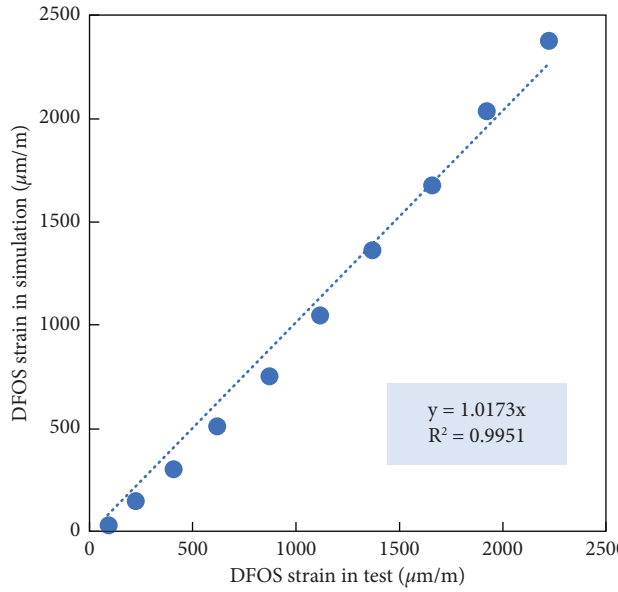

Figure 13: Linear relationship between the DFOS strain of the pure bending section in the laboratory test and numerical simulation.

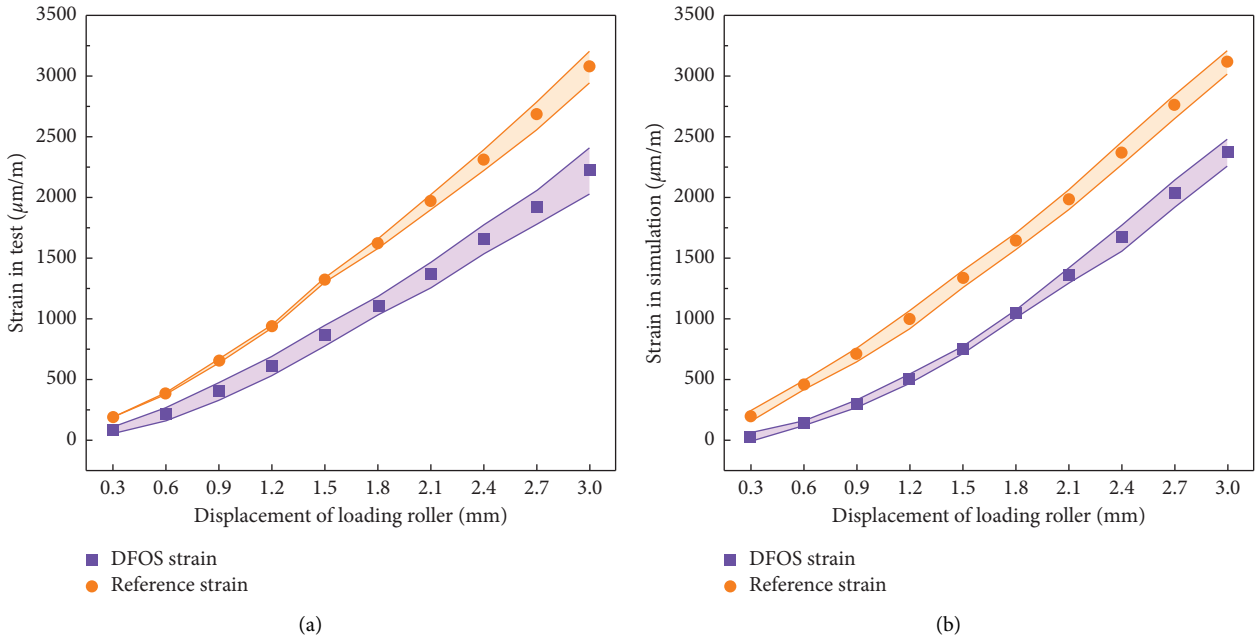

Figure 14: Strain of the pure bending section under different load levels. (a) Laboratory tests and (b) numerical simulations.

in Table 11. The higher the number of "∗," the more significant it is.

According to the results of the variance analysis shown in Table 11, the following conclusions were drawn. The elastic modulus showed significance ($F = 11.245$, $p = 0.007 < 0.05$), indicating that the elastic modulus has the main effect, which will have a significant effect on the strain correction coefficient. The effect of the section width ($F = 0.615$, $p = 0.630 > 0.05$) and section height ($F = 1.384$, $p = 0.335 > 0.05$) on the strain correction coefficient was less than that of the elastic modulus.

It can be observed from the results of the three-factor analysis of variance that the cross-sectional size has no significant influence on the strain correction coefficient. However, it can be seen from Table 9 that the influence of the cross-sectional size cannot be ignored. The reason for insignificance may be that the test error is large and the degree of freedom is small, resulting in low test sensitivity and covering the significance of the investigated factors. A large number of experiments are needed to study the effect of the section size on the strain correction coefficient.

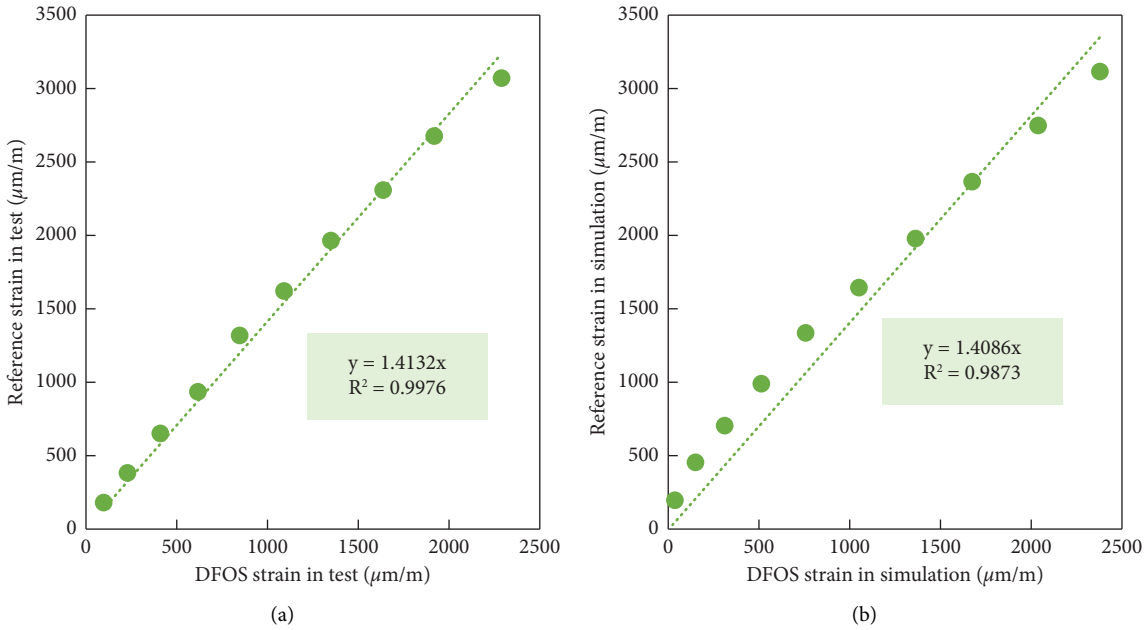

Figure 15: Linear relationship between the reference strain and the DFOS strain and its strain correction coefficient. (a) Laboratory tests and (b) numerical simulations.

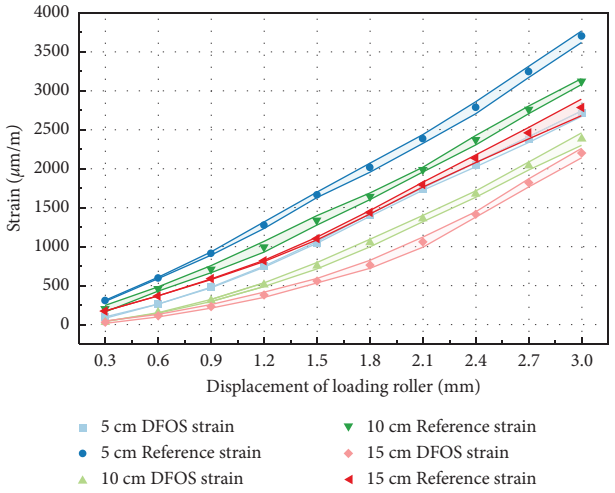

Figure 16: DFOS strain and reference strain under different loading roller distances.

5.3. Range Analysis. Range analysis was used to study the orthogonal test data, including the advantages between factors or the advantages and disadvantages of specific levels between factors. *K* value refers to the sum of test data for a certain factor at a certain level. *K*-avg value refers to the average value of the corresponding *K* value. *R* is the range of factors. The influence degree of each factor on the result can be compared according to the *R* value.

The range analysis was performed on test results, and the results are shown in Table 12. By observing the *R* values, it is found that the three factors affecting the DFOS are the elastic modulus, section height, and section width from high to low. The *K*-avg value of the strain correction coefficient is 0.99 when the elastic modulus is 1200 MPa. The *K*-avg values of the section width and section height are not much different, and the accuracy of the strain test decreases with the increase of the section size.

Combining the results of the range analysis and three-factor analysis of variance, it can be concluded that when the elastic modulus of the DFOS is close to the elastic modulus of the asphalt mixture, the accuracy of the sensor is higher which is consistent with the results of the previous research [23].

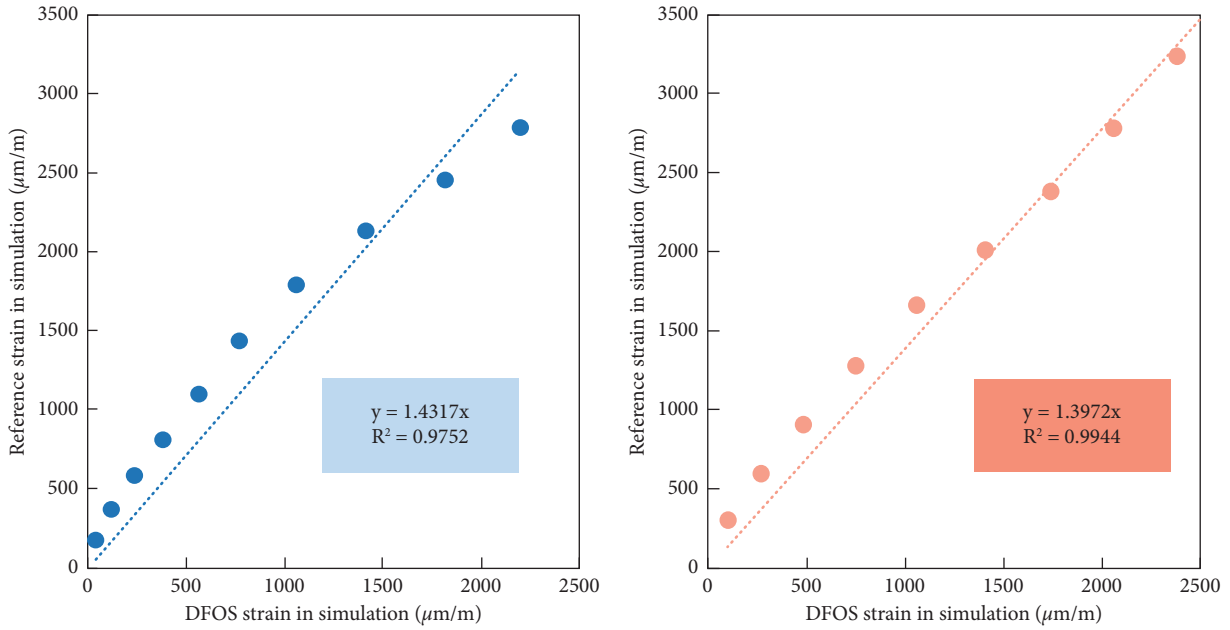

Figure 17: DFOS strain correction coefficient under different loading roller distances. (a) 5 cm and (b) 15 cm.

Table 8: Orthogonal test factors and levels.

Number	Elastic modulus (MPa)	Section width (mm)	Section height (mm)
1	300	4	4
2	1200	6	6
3	2100	8	8
4	3000	10	10

Table 9: Orthogonal test design and results.

Number	Elastic modulus (MPa)	Section width (mm)	Section height (mm)	Strain correction coefficient
1	300	4	4	0.6924
2	300	6	6	0.9705
3	300	8	8	1.2788
4	300	10	10	1.0992
5	1200	4	6	0.9791
6	1200	6	4	0.8572
7	1200	8	10	1.0688
8	1200	10	8	1.0739
9	2100	4	8	1.8508
10	2100	6	10	1.2576
11	2100	8	4	1.2509
12	2100	10	6	1.3842
13	3000	4	10	1.4822
14	3000	6	8	1.7423
15	3000	8	6	1.8784
16	3000	10	4	1.9766

Table 10: The calculation of each index in variance analysis.

Sources of variance	SS	df	MS	F
Elastic modulus (A)	$\sum_{i=1}^{a} n_{Ai}(\overline{y_{i\cdot}} - \overline{y})^2$	$a-1$	SSA/df$A$	MSA/MSE
Section width (B)	$\sum_{i=1}^{b} n_{Bi}(\overline{y_{i\cdot}} - \overline{y})^2$	$b-1$	SSB/df$B$	MSB/MSE
Section height (C)	$\sum_{i=1}^{c} n_{Ci}(\overline{y_{i\cdot}} - \overline{y})^2$	$c-1$	SSC/df$C$	MSC/MSE
Residual (E)	$\sum_{i=1}^{n}(\overline{y_i} - \overline{y})^2 - \mathrm{SS}A - \mathrm{SS}B - \mathrm{SS}C$	$n-1-\mathrm{df}A-\mathrm{df}B-\mathrm{df}C$	SSE/df$E$	

Table 11: Results of the three-factor analysis of variance.

Sources of variance	SS	df	MS	F	p
Elastic modulus	1.665	3	0.555	11.245	0.007**
Section width	0.091	3	0.030	0.615	0.630
Section height	0.205	3	0.068	1.384	0.335
Residual	0.296	6	0.049		
			R^2: 0.869		
			$^{**}p < 0.05$ $^{**}p < 0.01$		

Table 12: Results of range analysis.

	Level	Elastic modulus	Section width	Section height
K-avg value	1	1.01	1.25	1.19
	2	0.99	1.21	1.30
	3	1.44	1.37	1.49
	4	1.77	1.38	1.23
R		0.78	0.18	0.29

6. Conclusions

This study focused on the accuracy of DFOSs for asphalt pavement health monitoring. Based on the four-point bending test under static load, a coupling numerical simulation method of DEM-FDM is introduced. Compared with the traditional theoretical analysis and numerical simulation, it considers the material properties more comprehensively. Based on this method, the accuracy of the embedded DFOS for asphalt mixture strain testing was evaluated by analyzing the relationship between the reference strain and the DFOS strain, which greatly improves efficiency when compared with the indoor calibration test. Finally, orthogonal tests were designed to analyze the factors that influence the accuracy of the DFOSs for asphalt pavement health monitoring further. The following conclusions were obtained:

(1) The coupled DEM-FDM numerical simulation method can realize the simulation of asphalt mixture beam with the embedded distributed DFOS, which was verified by laboratory tests with high accuracy.

(2) The strain of the embedded DFOS has a good linear relationship with the reference strain. In laboratory tests and numerical simulations, the slope of the linear fitting is the strain correction coefficient. Strain correction can effectively improve the accuracy of DFOS for asphalt mixture testing.

(3) The strain correction coefficients obtained from DEM-FDM simulations are similar to those measured in laboratory tests. In the study of DFOS for asphalt mixture health monitoring, DEM-FDM coupled numerical simulation can be used as a new strain correction method.

(4) The elastic modulus, section height, and section width of the DFOS affect its testing accuracy for asphalt mixture. Among them, the influence of elastic modulus is a significant effect, while the influence of section height and width is weak. When the elastic modulus of DFOS is similar to that of the asphalt mixture, the accuracy of the DFOS is higher.

In summary, this study presents a preliminary strain correction method to ensure accurate measurement of DFOSs in asphalt mixtures. For more complex test conditions, such as dynamic loads and different test temperatures, the numerical simulation should be further enriched. Furthermore, this method can also be used to optimize the development and design of DFOSs for pavement response monitoring.

Data Availability

The data used to support the findings of this study are available from the corresponding author upon request.

Disclosure

Any statement, opinion, finding, and conclusion of this paper reflect the views of the authors and do not necessarily reflect those of the sponsoring agencies.

Conflicts of Interest

The authors declare that they have no conflicts of interest.

Acknowledgments

This work was supported by the National Key Research and Development Program of China (2018YFB1600100). This work was also supported by the National Natural Science Foundation of China (U20A20315 and 52008139), China Postdoctoral Science Foundation (2022T150165, 2020M670915), Heilongjiang Provincial Postdoctoral Science Foundation (LBH-Z19222), and Jilin Provincial Department of Transportation Science and Technology Project (2020-1-10). Fundamental Research Funds for the Central Universities. The authors also appreciate the cooperation with Jilin Provincial Transportation Planning and Design Institute.

References

[1] A. Shtayat, S. Moridpour, B. Best, A. Shroff, and D. Raol, "A review of monitoring systems of pavement condition in paved and unpaved roads," *Journal of Traffic and Transportation Engineering*, vol. 7, no. 5, pp. 629–638, 2020.

[2] W. Liu, H. Wang, Z. Zhou, X. Xing, D. Cao, and Z. Jiang, "Optical fiber-based sensors with flexible encapsulation for pavement behavior monitoring: optical fiber-based sensors for pavement monitoring," *Structural Control and Health Monitoring*, vol. 22, no. 2, pp. 301–313, 2015.

[3] P. G. Hubbard, R. Ou, and T. Xu, "Road deformation monitoring and event detection using asphalt-embedded distributed acoustic sensing (DAS)," *Structural Health Monitoring*, vol. 17, 2022.

[4] H.-N. Li, D.-S. Li, and G.-B. Song, "Recent applications of fiber optic sensors to health monitoring in civil engineering," *Engineering Structures*, vol. 26, no. 11, pp. 1647–1657, 2004.

[5] J. M. Henault, J. Salin, and G. Moreau, "Monitoring of concrete structures using OFDR technique," *AIP Conference Proceedings*, vol. 1335, pp. 1386–1393, 2011.

[6] A. Barrias, J. R. Casas, and S. Villalba, "Fatigue performance of distributed optical fiber sensors in reinforced concrete elements," *Construction and Building Materials*, vol. 218, pp. 214–223, 2019.

[7] C. Lan, Z. Zhou, and J. Ou, "Monitoring of structural prestress loss in RC beams by inner distributed Brillouin and fiber Bragg grating sensors on a single optical fiber: methodology and component of monitoring prestress loss," *Structural Control and Health Monitoring*, vol. 21, no. 3, pp. 317–330, 2014.

[8] X. Tan, A. Abu-Obeidah, Y. Bao, H. Nassif, and W. Nasreddine, "Measurement and visualization of strains and cracks in CFRP post-tensioned fiber reinforced concrete beams using distributed fiber optic sensors," *Automation in Construction*, vol. 124, Article ID 103604, 2021.

[9] S. Zhang, H. Liu, A. A. S. Coulibaly, and M. DeJong, "Fiber optic sensing of concrete cracking and rebar deformation using several types of cable," *Structural Control and Health Monitoring*, vol. 28, no. 2, p. e2664, 2021.

[10] M. F. Bado, J. R. Casas, and G. Kaklauskas, "Distributed sensing (DOFS) in reinforced concrete members for reinforcement strain monitoring, crack detection and bond-slip calculation," *Engineering Structures*, vol. 226, Article ID 111385, 2021.

[11] F. Tang, L. Zhao, H. Tian, H. N. Li, and H. Li, "Localization and monitoring of initiation and propagation of corrosion-induced mortar cracking based on OFDR distributed optical fiber sensor," *Journal of Intelligent Material Systems and Structures*, vol. 32, no. 17, pp. 1948–1965, 2021.

[12] L. Meng, L. Wang, Y. Hou, and G. Yan, "A research on low modulus distributed fiber optical sensor for pavement material strain monitoring," *Sensors*, vol. 17, no. 10, p. 2386, 2017.

[13] P. Xiang and H. Wang, "Optical fibre-based sensors for distributed strain monitoring of asphalt pavements," *International Journal of Pavement Engineering*, vol. 19, no. 9, pp. 842–850, 2018.

[14] A. Barrias, J. R. Casas, and S. Villalba, "Distributed optical fibre sensors in concrete structures: performance of bonding adhesives and influence of spatial resolution," *Structural Control and Health Monitoring*, vol. 26, no. 3, p. e2310, 2019.

[15] H. Wang, L. Jiang, and P. Xiang, "Priority design parameters of industrialized optical fiber sensors in civil engineering," *Optics & Laser Technology*, vol. 100, pp. 119–128, 2018.

[16] H. Wang, P. Xiang, and L. Jiang, "Strain transfer theory of industrialized optical fiber-based sensors in civil engineering: a review on measurement accuracy, design and calibration," *Sensors and Actuators A: Physical*, vol. 285, pp. 414–426, 2019.

[17] A. Bassil, X. Chapeleau, D. Leduc, and O. Abraham, "Concrete crack monitoring using a novel strain transfer model for distributed fiber optics sensors," *Sensors*, vol. 20, no. 8, p. 2220, 2020.

[18] I. Alj, M. Quiertant, A. Khadour et al., "Experimental and numerical investigation on the strain response of distributed optical fiber sensors bonded to concrete: influence of the adhesive stiffness on crack monitoring performance," *Sensors*, vol. 20, no. 18, p. 5144, 2020.

[19] H. Wang and P. Xiang, "Strain transfer analysis of optical fiber based sensors embedded in an asphalt pavement structure," *Measurement Science and Technology*, vol. 27, no. 7, Article ID 075106, 2016.

[20] L. Yuan and L. Zhou, "Sensitivity coefficient evaluation of an embedded fiber-optic strain sensor," *Sensors and Actuators A: Physical*, vol. 69, no. 1, pp. 5–11, 1998.

[21] G. Luyckx, E. Voet, W. De Waele, and J. Degrieck, "Multi-axial strain transfer from laminated CFRP composites to embedded Bragg sensor: I. Parametric study," *Smart Materials and Structures*, vol. 19, no. 10, Article ID 105017, 2010.

[22] Z. X. Li, G. Y. Hou, T. Hu, T. Zhou, and H. Xiao, "Study on establishing and testing for strain transfer model of distributed optical fiber sensor in concrete structures," *Optical Fiber Technology*, vol. 61, Article ID 102430, 2021.

[23] Z. Dong, X. Ma, X. Gong, and M. Oeser, "Theoretical evaluation of the measurement accuracy of fiber Bragg grating strain sensors within randomly filled asphalt mixtures based on finite element simulation," *Structural Control and Health Monitoring*, vol. 25, no. 1, p. e2057, 2018.

[24] X. F. Zhang, Z. D. Qian, M. Zhang, and L. Chen, "Numerical simulation for synergetic deformation of optical fiber sensor and asphalt mixture," *KSCE Journal of Civil Engineering*, vol. 23, no. 7, pp. 3075–3087, 2019.

[25] T. Bao, J. Li, X. Zhu, and C. Gu, "Analysis of strain transfer between surface-bonded plastic optical fibers and concrete," *Optical Engineering*, vol. 58, no. 2, p. 1, 2019.

[26] X. Ma, Z. Dong, F. Chen, H. Xiang, C. Cao, and J. Sun, "Airport asphalt pavement health monitoring system for mechanical model updating and distress evaluation under realistic random aircraft loads," *Construction and Building Materials*, vol. 226, pp. 227–237, 2019.

[27] X. Ma, Z. Dong, X. Yu, F. Chen, C. Cao, and J. Sun, "Monitoring the structural capacity of airfield pavement with built-in sensors and modulus back-calculation algorithm," *Construction and Building Materials*, vol. 175, pp. 552–561, 2018.

[28] X. Ma, W. Quan, Z. Dong, Y. Dong, and C. Si, "Dynamic response analysis of vehicle and asphalt pavement coupled system with the excitation of road surface unevenness," *Applied Mathematical Modelling*, vol. 104, pp. 421–438, 2022.

[29] Z. Dong, X. Ma, and X. Shao, "Airport pavement responses obtained from wireless sensing network upon digital signal processing," *International Journal of Pavement Engineering*, vol. 19, no. 5, pp. 381–390, 2018.

[30] X. Ma, Z. Dong, and Y. Dong, "Toward asphalt pavement health monitoring with built-in sensors: a novel application to real-time modulus evaluation," *IEEE Transactions on Intelligent Transportation Systems*, pp. 1–13, 2021.

[31] C. Shi, C. Zhao, X. Zhang, and Y. Guo, "Coupled discrete-continuum approach for railway ballast track and subgrade macro-meso analysis," *International Journal of Pavement Engineering*, vol. 22, no. 13, pp. 1744–1759, 2021.

[32] C. Shi and Z. Chen, "Coupled DEM/FDM to evaluate track transition stiffness under different countermeasures," *Construction and Building Materials*, vol. 266, Article ID 121167, 2021.

[33] B. Indraratna, N. T. Ngo, C. Rujikiatkamjorn, and S. W. Sloan, "Coupled discrete element–finite difference method for analysing the load-deformation behaviour of a single stone column in soft soil," *Computers and Geotechnics*, vol. 63, pp. 267–278, 2015.

[34] Z. Xu, L. Zhang, and S. Zhou, "Influence of encasement length and geosynthetic stiffness on the performance of stone column: 3D DEM-FDM coupled numerical investigation," *Computers and Geotechnics*, vol. 132, Article ID 103993, 2021.

[35] JTG F40-2004, *Technical Specifications for Construction of Highway Asphalt Pavements*, Ministry of Transport of the People's Republic of China, Beijing, China, 2004.

[36] J. Huang, J. Pei, Y. Li et al., "Investigation on aggregate particles migration characteristics of porous asphalt concrete (PAC) during vibration compaction process," *Construction and Building Materials*, vol. 243, Article ID 118153, 2020.

[37] Y. Jiang, C. Deng, J. Xue, H. Liu, and Z. Chen, "Investigation of the fatigue properties of asphalt mixture designed using vertical vibration method," *Road Materials and Pavement Design*, vol. 21, no. 5, pp. 1454–1469, 2020.

[38] A. Sounthararajah, L. Wong, N. Nguyen, H. H. Bui, and J. Kodikara, "Evaluation of flexural behaviour of cemented pavement material beams using distributed fibre optic sensors," *Construction and Building Materials*, vol. 156, pp. 965–975, 2017.

[39] Z. Liu and Y. Wang, "Laboratory research on asphalt mastic modified with activated carbon powder: rheology, microstructure, and adhesion," *Road Materials and Pavement Design*, vol. 22, no. 6, pp. 1424–1441, 2021.

[40] T. Ma, D. Zhang, Y. Zhang, S. Wang, and X. Huang, "Simulation of wheel tracking test for asphalt mixture using discrete element modelling," *Road Materials and Pavement Design*, vol. 19, no. 2, pp. 367–384, 2018.

[41] J. Du, D. Ren, C. Ai, J. Zhang, and Y. Qiu, "Effect of aggregate gradation on crack propagation in asphalt mixtures at low temperatures based on the Eshelby equivalent inclusion theory," *Construction and Building Materials*, vol. 290, Article ID 123181, 2021.

[42] D. Zhang, L. Gu, and J. Zhu, "Effects of aggregate mesostructure on permanent deformation of asphalt mixture using three-dimensional discrete element modeling," *Materials*, vol. 12, no. 21, p. 3601, 2019.

[43] G. Liu, D. Han, C. Zhu, F. Wang, and Y. Zhao, "Asphalt-mixture force chains length distribution and skeleton composition investigation based on computational granular mechanics," *Journal of Materials in Civil Engineering*, vol. 33, no. 4, Article ID 04021033, 2021.

[44] X. Chen, C. Ai, J. Du, H. He, and Y. Huang, "Effect of gradation segregation on low-temperature crack resistance of asphalt pavement using 3D DEM," *Construction and Building Materials*, vol. 274, Article ID 122060, 2021.

[45] A. O. Sojobi, D. Xuan, L. Li, S. Liu, and C. S. Poon, "Optimization of gas-solid carbonation conditions of recycled aggregates using a linear weighted sum method," *Developments in the Built Environment*, vol. 7, Article ID 100053, 2021.

[46] A. O. Sojobi and K. M. Liew, "Flexural behaviour and efficiency of CFRP-laminate reinforced recycled concrete beams: optimization using linear weighted sum method," *Composite Structures*, vol. 260, Article ID 113259, 2021.